The impact of silicon on the solidification of duplex lightweight steels

Tilen Balaško[1] · Jaka Burja[1,2] · Jožef Medved[1]

Abstract

Efforts are being made worldwide to transform road transport to minimise its contribution to greenhouse gas emissions, with a focus on reducing vehicle mass. Lightweight manganese–aluminium steels have gained popularity for this purpose due to their low density and combination of strength and plasticity. In this particular study, the solidification process of five lightweight manganese–aluminium steels with different silicon content was investigated. The steels were fabricated by inductive melting in a vacuum and remelted during further thermal analysis. A reference steel composition (Fe-14Mn-10Al-0.2Si-0.8C) was used, and the remaining four steels contained different amounts of silicon (0.5, 1.0, 2.0 and 4.0 mass%). The impact of silicon on solidification was analysed by thermodynamic calculations (CALPHAD method), differential thermal analysis and optical microscopy. The thermodynamic calculations gave good estimates for the liquidus and austenite liquidus temperatures, but higher solidus temperatures than the experimental results. The presence of silicon decreases the density and lowers the solidus and liquidus temperatures, resulting in a prolonged solidification interval. In addition, the spacing of the secondary dendrite arms decreases, except at a silicon concentration of 0.5 mass%, where an increase was observed compared to the reference steel.

Keywords Lightweight steels · Duplex steels · Solidification · DTA · CALPHAD

Introduction

Protecting the environment is becoming increasingly important as we face a growing world population, new advances in technology and rising purchasing power, leading to an increase in production and consequently consumption [1–3]. A crucial increase in greenhouse gas (GHG) emissions has been caused mainly by human activities [1, 4]. Fossil fuel combustion for heating, electricity and transport are the main activities leading to an increase in GHG emissions [1, 5]. Transport is known to have the largest impact on GHG emissions [1], with road transport standing out as one of the main sources of GHG emissions [6, 7]. GHG emissions from transport have a direct impact on carbon emissions, climate change and human well-being [1, 8]. Globally, GHG emissions continue to rise, with the transport sector being the largest

contributor [9, 10]. Approximately 20% of GHG emissions in the European Union originate from the transport sector, with 72% of these emissions attributed to road transport [11, 12]. There are calls worldwide to reduce GHG emissions from road transport [13, 14]. This can be achieved by reducing the mass of vehicles [15–17]. One way to achieve this is to use newly developed materials with lower density, e.g., lightweight manganese–aluminium steels. The steels mentioned above are interesting due to their low specific weight combined with good mechanical properties [18–28]. Lightweight manganese–aluminium steels are categorised according to their main structural constituent, i.e. ferrite, ferrite–austenite and austenite [18, 20, 22]. The addition of silicon can replace the aluminium content, but the density does not increase, but decreases slightly, because the density of silicon is lower than that of aluminium. The reason for this is that a higher aluminium content reduces the ductility of steels because κ-carbide precipitates, which forms susceptible sites for cracking during deformation [29]. The influence of silicon in lightweight steels has already been discussed [29], but not the solidification process. The microstructure in the as-cast state affects reheating and hot working, leading to poor final properties or processing failure.

✉ Tilen Balaško
tilen.balasko@ntf.uni-lj.si

1 Faculty of Natural Sciences and Engineering, University of Ljubljana, Aškerčeva Cesta 12, 1000 Ljubljana, Slovenia

2 Institute of Metals and Technology, Lepi Pot 11, 1000 Ljubljana, Slovenia

The solidification of lightweight steels has a significant impact on their microstructure and further processing. In this study, the impact of silicon on the solidification of lightweight duplex (ferrite–austenite) steels was investigated. Thermodynamic calculations were made using Thermo-Calc software to understand the impact of silicon on solidification. Five lightweight duplex steels with different silicon contents were prepared and remelted with a STA (simultaneous thermal analyser—NETZSCH STA 449 C Jupiter). The first sample was Fe-14Mn-10Al-0.2Si-0.8C (mass%), while the rest had increased silicon contents (0.5, 1.0, 2.0 and 4.0 mass% Si—the samples were designated 1, 2, 3 and 4, respectively). The sample Fe-14Mn-10Al-0.2Si-0.8C served as a reference (sample 0) to investigate the impact of silicon on the solidification process. A comparison was made between the experimental values and the thermodynamic calculations.

Experimental work

Materials

Batches of steel weighing 6 kg were vacuum inductively melted under an inert argon atmosphere to prevent oxidation. The molten steel was then cast into an ingot of $60 \times 60 \times 250$ mm, using pure elements such as aluminium, manganese, silicon, carbon and mild steel. To achieve homogeneity, the ingots were subjected to a homogenisation treatment at a temperature of 1150 °C for a duration of 2 h. The chemical composition of the samples (Table 1) was determined by wet analysis and infrared absorption techniques after combustion, using an ELTRA CS-800 instrument. To perform the differential thermal analysis (DTA), the samples were cut 100 mm below the top of the ingot and 15 mm below the surface.

Thermodynamic calculations

For the thermodynamic calculations with the CALPHAD method, the software Thermo-Calc 2022b [30] was used. To acquire the necessary thermodynamic data, the TCFE10

Steels/Fe-alloys database was used [31]. For simulating the process of solidification, the equilibrium method was employed. The one-axis calculation diagram was selected for the equilibrium calculator, enabling the generation of diagrams illustrating the variations in characteristic temperatures and stable phases during the solidification process. Furthermore, Thermo-Calc was employed to determine the density of the samples under investigation.

Differential thermal analysis (DTA)

Differential thermal analysis (DTA) was performed using the NETZSCH STA 449 C Jupiter thermal analyser. The samples were subjected to heat up to a temperature of 1550 °C and then cooled down to room temperature while being protected by argon gas. The heating and cooling rate was 10 K min^{-1}. Empty Al_2O_3 crucibles were used as reference. To ensure uniformity, the samples were cut into cylinders with a height of 3 mm (± 0.1 mm) and a diameter of 4 mm (± 0.1 mm). The mass of the samples varied between 220 and 320 mg. The obtained cooling curves were analysed to examine the solidification process of the lightweight duplex steels. We applied the DTA method to obtain the characteristic solidification temperatures. It is worth mentioning that DTA or differential scanning calorimetry (DSC) has been used in numerous research papers to study the characteristic temperatures, such as liquidus and solidus, of different metal alloys [32–34].

Principle of density determination

The density of the samples was calculated using Archimedes' principle and a KERN ALJ 220-4MN balance. The formula used for this calculation was Eq. (1):

$$\rho = \frac{A}{A - B}\rho_0 \tag{1}$$

where ρ is the density of the sample, A is the mass of the sample in air, B is the mass of the sample in the measuring liquid and ρ_0 is the density of the measuring liquid (distilled water). To ensure accuracy, a total of 8 measurements were

Table 1 The composition of the analysed samples (mass%)

Sample	C	Si	Mn	P	S	Cu	Ni	Al	Fe
0	0.81	0.20	14.00	0.009	0.007	0.17	0.43	10.10	Bal.
1	0.81	0.50	14.00	0.008	0.006	0.17	0.46	9.80	Bal.
2	0.82	1.00	13.90	0.009	0.007	0.18	0.48	9.90	Bal.
3	0.82	2.00	14.00	0.008	0.007	0.17	0.47	10.00	Bal.
4	0.81	4.00	13.90	0.009	0.007	0.18	0.49	9.80	Bal.

taken. The lowest and highest values obtained from these measurements were excluded for the calculation of the average density of the samples.

Metallography

Preparation of the samples for metallography included grinding, polishing and etching using a 10% Nital solution by mass. A Nikon Microphot FXA optical microscope equipped with a Hitachi HV-C20A 3CCD video camera was used for metallography.

Results and discussion

Thermodynamic calculations

Table 2 contains the thermodynamically calculated liquidus, solidus, austenite liquidus temperatures and solidification intervals (ΔT) of the investigated samples. Figure 1 shows the mass fraction of the stable phases in the temperature range from 1200 to 1450 °C for the investigated samples, namely melt (liquid phase), δ-ferrite (BCC_A2), body centred cubic ordered phase (BCC_B2), austenite, and MnS. MnS occurs in small quantities because of the low sulphur (~ 0.007 mass%) and exerts no significant influence on the solidification process. There are two body centred cubic phases, the first (BCC_A2) is a metastable disordered δ-ferrite (high-temperature phase) and the second (BCC_B2) is a stable ordered body centred phase (low-temperature phase), the latter only occurring in sample 4 in the temperature range studied. The liquidus temperatures (at a δ-ferrite mass fraction of 0) were 1411, 1406, 1394, 1371 and 1325 °C for samples 0, 1, 2, 3 and 4, respectively. The austenite liquidus temperatures were 1305, 1301, 1290, 1271 and 1234 °C for samples 0, 1, 2, 3 and 4, respectively. On the other hand, the solidus temperatures (when the mass fraction of the liquid phase is 0) were 1299, 1288, 1276, 1254 and 1210 °C (Table 2) for samples 0, 1, 2, 3 and 4, respectively. There is a visible trend with the addition of

Table 2 Calculated characteristic solidification temperatures

Sample	Liquidus/°C	Austenite liquidus/°C	Solidus/°C	Solidification interval—ΔT/°C
0	1411	1305	1299	112
1	1406	1301	1288	118
2	1394	1290	1276	118
3	1371	1271	1254	117
4	1325	1234	1210	115

silicon where the liquidus, austenite liquidus and solidus temperatures decrease with increasing silicon content, but the solidification interval remains almost the same: 112 °C for sample 0 to 115 °C for sample 4 (Table 2). It increases only slightly at the highest silicon content (115 °C for sample 4) and is greatest for samples 1 and 2 (118 °C), but the changes are very small.

Based on the thermodynamic calculations, several conclusions can be drawn regarding the solidification process. Samples 0, 1, 2 and 3 (Fig. 1) solidify in the following order: (1) L→L+δ-ferrite, (2) L→L+δ-ferrite+austenite and (3) L→δ-ferrite+austenite. As already stated, the temperatures vary with the addition of silicon, as indicated in Table 2. Sample 4 (Fig. 1e) undergoes a bit different solidification process. Based on the calculations, the solidification can be described in the following order: (1) L→L+δ-ferrite (BCC_A2), (2) L→L+δ-ferrite (BCC_A2)+austenite, (3) L→L+body centred ordered phase (BCC_B2)+austenite and (4) L→body centred ordered phase (BCC_B2)+austenite. Under these circumstances, Thermo-Calc predicts a transformation of ferrite from δ-ferrite (BCC_A2) to the body centred ordered phase (BCC_B2) during the solidification process. This transformation starts at 1212 °C (which is slightly above the solidus temperature of 1210 °C) and ends at 1209 °C. The δ-ferrite transformations in the other samples investigated (samples 0, 1, 2 and 3) take place at lower temperatures and therefore do not significantly affect the overall solidification process.

Differential thermal analysis

Figure 2 shows the cooling curves obtained from the samples examined. The results of the DTA show the presence of two peaks during solidification. The formation of δ-ferrite (solidification of δ-ferrite) is identified as the first peak, while the second peak marks the formation of austenite (austenite liquidus temperature). The liquidus temperatures for the samples are shown in Table 3, with no evidence of MnS formation. The liquidus temperatures (solidification of δ-ferrite) were 1404.3, 1405.0, 1378.5, 1348.2, and 1310.7 °C for samples 0, 1, 2, 3, and 4, respectively. The austenite liquidus temperature, i.e. the starting temperature of austenite solidification, was 1308.8, 1306.1, 1265.3, 1226.1, and 1209.8 °C for samples 0, 1, 2, 3, and 4 respectively. On the other hand, the solidus temperatures were 1273.7, 1247.9, 1190.4, 1158.3, and 1091.7 °C for samples 0, 1, 2, 3, and 4, respectively. There are some visible differences in the solidification of sample 4 (Fig. 2e) compared to the other samples (Fig. 2a–d). First, the peak at the beginning of austenite liquidus, i.e. the beginning of austenite solidification, is slightly lower (Fig. 2e−1209.8 °C) and the third peak marks the
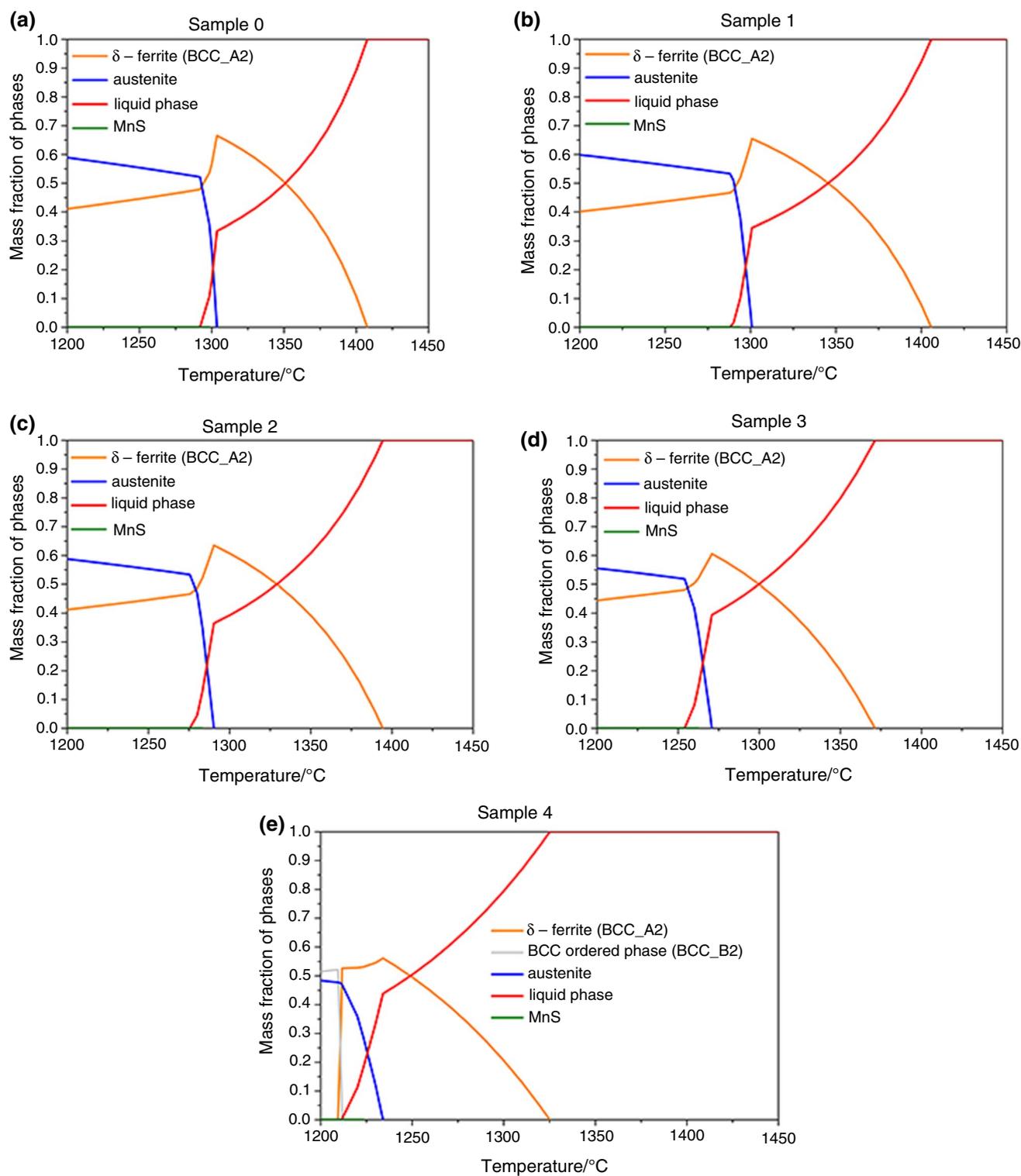
Fig. 1 Mass fraction of the phases in equilibrium in relation to the temperature for sample 0 (**a**), sample 1 (**b**), sample 2 (**c**), sample 3 (**d**) and sample 4 (**e**). (Color figure online)

transformation of ferrite from δ-ferrite (BCC_A2) to body centred ordered phase (BCC_B2) during solidification, which starts at 1171.8 °C and ends at 1162.2 °C.

The experimental solidification intervals differ from the calculated ones, where there were only minor changes, with the largest difference being 4 °C. In fact, the solidification

Fig. 2 The cooling curves obtained by DTA for sample 0 (**a**), sample 1 (**b**), sample 2 (**c**), sample 3 (**d**) and sample 4 (**e**). (Color figure online)

Table 3 Characteristic solidification temperatures of the studied samples, determined with DTA

Sample	Liquidus/°C	Austenite liquidus/°C	Solidus/°C	Solidification interval—ΔT/°C
0	1404.3	1308.8	1273.7	130.6
1	1405.0	1306.1	1247.9	157.1
2	1378.5	1265.3	1190.4	188.1
3	1348.2	1226.1	1158.3	189.9
4	1310.7	1209.8	1091.7	219.0

intervals increase with the addition of silicon and range from 130.6 °C (sample 0) to 219.0 °C (sample 4—Table 3). The results of the study have important implications for industrial use. The lightweight duplex steels studied can potentially be used in the automotive industry. Continuous casting is desirable for high production tonnages, but steels with higher silicon content (above 2.0 mass%) are not suitable due to their long solidification intervals of above 200 °C. Instead, they are better suited for ingot casting or cast production.
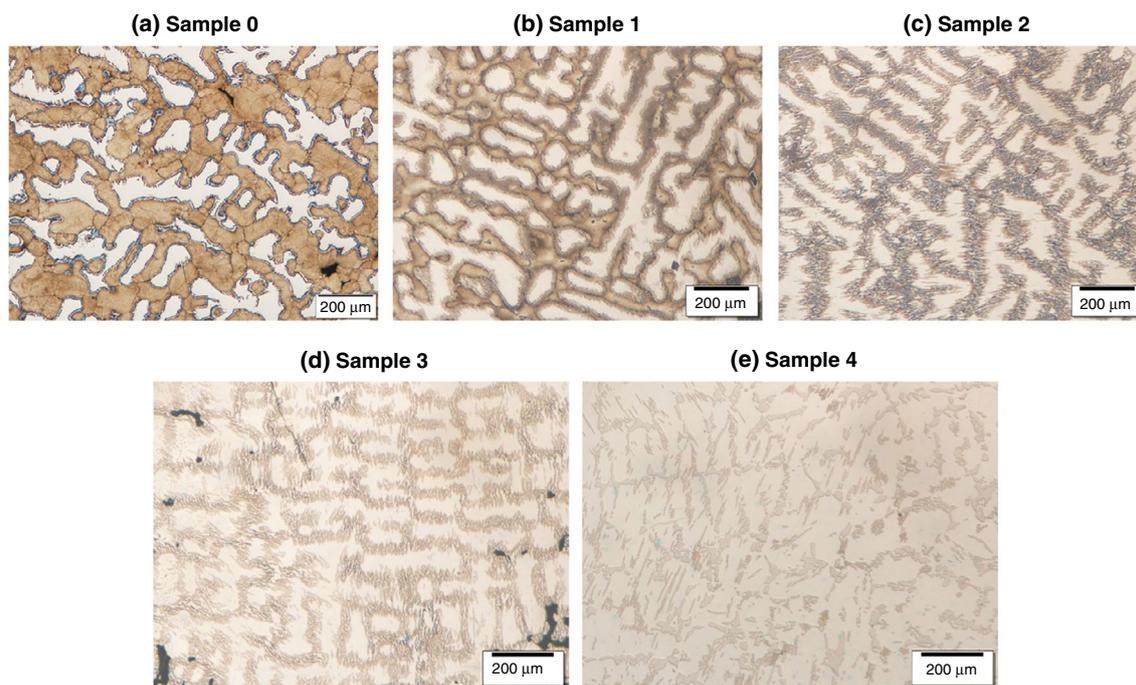
Fig. 3 The microstructure of the samples after DTA is shown as follows: sample 0 (**a**), sample 1 (**b**), sample 2 (**c**), sample 3 (**d**) and sample 4 (**e**). (Color figure online)

The amount of energy released during solidification was 46.28, 79.36, 93.93, 102.98 and 168.55 J g^{-1} for samples 0, 1, 2, 3 and 4 respectively. The more silicon is added, the more total energy is emitted during solidification. Sample 4 stands out as the total energy emitted is 168.55 J g^{-1} (3.6× higher than the reference sample 0). The largest contributions are the transformation of δ-ferrite (BCC_A2) into a body centred ordered phase (BCC_B2) and the longer solidification interval.

The solidification process observed in the first four samples (samples 0, 1, 2 and 3) remained consistent, but differed in sample 4. The increase in silicon content led to a decrease in the formation temperature of δ-ferrite (liquidus—Table 3) and austenite (austenite liquidus—Table 3), as well as the solidus temperature. The thermodynamic calculations accurately predicted the solidification temperature of δ-ferrite and austenite, except for the solidus temperature and solidification interval, which showed some deviations from the DTA results. The calculated results showed that the solidification interval did not change significantly with the addition of silicon. However, the DTA results showed an increase in the solidification interval from 130.6 °C (sample 0) to 219.0 °C (sample 4) with increasing silicon content. Furthermore, the calculations indicated that the ferrite transformation (δ-ferrite (BCC_A2) to the body centred ordered phase (BCC_B2)) could influence the solidification process, which was confirmed by the DTA results (Fig. 2e).

Metallography

The DTA samples show a microstructure composed of δ-ferrite and austenite, with the presence of precipitated carbides. In the micrographs (Fig. 3), the lighter phase corresponds to the δ-ferrite, while the darker phase represents the austenite (Fig. 3). The δ-ferrite exhibits the typical dendritic structure in the as-cast state. The content of δ-ferrite increases with higher silicon content in the samples. Upon the optical microscopy examination, sample 1 was found to contain 36.40 vol% ferrite, sample 2 41.34 vol%, sample 3 67.18 vol% and sample 4 80.05 vol% ferrite. Ferrite has a body-centred cubic crystal lattice, which contributes to the lower density of the samples compared to reference sample 0.

SDAS measurements

The secondary dendrite arm spacing (SDAS) was measured by optical microscopy. This was done using Eq. 2, which goes back to a previous study [35].

$$\text{SDAS} = \frac{L}{N-1} \tag{2}$$

where N represents the number of secondary dendrite arms along one side of the primary arm, and L is the length

Table 4 The values represent the measured SDAS for each sample

Sample	SDAS/μm
0	80.1
1	94.3
2	73.7
3	75.9
4	56.0

Table 5 Examined sample densities: measured and calculated

Sample	Measured ρ kg^{-1} m^{-3}	Calculated ρ kg^{-1} m^{-3}
0	6702	6797
1	6540	6819
2	6553	6825
3	6547	6790
4	6542	6718

parallel to the primary arm [35]. The results of the secondary dendrite arm spacing (SDAS) measurements are summarised in Table 4.

The SDAS results show that the presence of silicon alters the spacing between dendrite arms. The addition of 0.5 mass% silicon (sample 1) increases the SDAS by 14.3 μm, while all higher additions of silicon decrease the SDAS. With 1.0 mass% silicon (sample 2), the SDAS decreases at 6.4 μm, with 2.0 mass% silicon (sample 3) at 4.2 μm (almost the same difference as sample 2) and with 4.0 mass% silicon (sample 4) at 24.1 μm.

Density of the samples

The results of the calculated and measured densities are shown in Table 5. The measured densities span from 6702 to 6540 kg m^{-3} and are lower than the densities calculated by Thermo-Calc. The best agreement is observed for sample 0, where the calculated density differs from the measured density by only 95 kg m^{-3}. The average of the other experimental values is 6546 kg m^{-3} and for the calculated value 6788 kg m^{-3}. The addition of silicon leads to a decrease in density compared to the sample without silicon addition (sample 0). Furthermore, the density decreases further with the addition of 2.0 mass% silicon (sample 3) and beyond, which is primarily due to the higher ferrite content in these samples.

Conclusions

Thermodynamic calculations were used to determine the solidification process of duplex lightweight steels with increasing silicon content. While the measured liquidus temperatures agreed well, the solidus temperatures deviated more, especially at higher silicon contents.

The addition of silicon increases the solidification interval by 26.5 °C (sample 1—0.5 mass% silicon), 57.5 °C (sample 2—1 mass% silicon), 59.3 °C (sample 3—2 mass% silicon) and 88.4 °C (sample 4—4 mass% silicon), i.e. the solidification interval ranges from 130.6 °C in the case of sample 0 to 219.0 °C in the case of sample 4. Due to the wide solidification ranges of the 4 mass% silicon additions to sample 0, they are only suitable for ingot casting or as-cast products.

On the other hand, the density of the investigated samples with silicon addition was reduced compared to the reference sample 0. Above 1.0 mass% silicon, the density starts to decrease even more, as the ferrite content increases from 41.34 vol% (sample 2) to 80.05 vol% ferrite (sample 4).

Declarations

References

1. Kazancoglu Y, Ozbiltekin-Pala M, Ozkan-Ozen YD. Prediction and evaluation of greenhouse gas emissions for sustainable road transport within Europe. Sustain Cities Soc. 2021;70:102924. https://doi.org/10.1016/j.scs.2021.102924.

2. Wang R, Mirza N, Vasbieva DG, Abbas Q, Xiong D. The nexus of carbon emissions, financial development, renewable energy consumption, and technological innovation: what should be the priorities in light of COP 21 Agreements? J Environ Manage. 2020;271:111027. https://doi.org/10.1016/j.jenvman.2020.111027.

3. Davis M, Ahiduzzaman M, Kumar A. How will Canada's greenhouse gas emissions change by 2050? A disaggregated analysis of past and future greenhouse gas emissions using bottom-up energy modelling and Sankey diagrams. Appl Energy. 2018;220:754–86. https://doi.org/10.1016/j.apenergy.2018.03.064.

4. Basha G, Kishore P, Ratnam MV, Jayaraman A, Kouchak AA, Ouarda TBMJ, et al. Historical and projected surface temperature over India during the 20th and 21st century. Sci Rep. 2017. https://doi.org/10.1038/s41598-017-02130-3.

5. Perera F. Pollution from fossil-fuel combustion is the leading environmental threat to global pediatric health and equity: solutions exist. Int J Environ Res Public Health. 2018. https://doi.org/10.3390/ijerph15010016.

6. Kijewska K, Iwan S, Korczak J. Challenges to increase the sustainable urban freight transport in South Baltic Region–LCL project. Transp Res Procedia. 2019;39:170–9. https://doi.org/10.1016/j.trpro.2019.06.019.

7. Thompson RG, Nassir N, Frauenfelder P. Shared freight networks in metropolitan areas. Transp Res Procedia. 2020;46:204–11. https://doi.org/10.1016/j.trpro.2020.03.182.

8. Bain PG, Milfont TL, Kashima Y, Bilewicz M, Doron G, Garoarsdóttir RB, et al. Co-benefits of addressing climate change can motivate action around the world. Nat Clim Chang. 2016;6:154–7. https://doi.org/10.1038/nclimate2814.

9. Lu X, Ota K, Dong M, Yu C, Jin H. Predicting transportation carbon emission with urban big data. IEEE Trans Sustain Comput. 2017;2:333–44. https://doi.org/10.1109/TSUSC.2017.2728805.

10. Bleviss DL. Transportation is critical to reducing greenhouse gas emissions in the United States. Wiley Interdiscip Rev Energy Environ. 2021;10:1–16. https://doi.org/10.1002/wene.390.

11. Ajanovic A, Haas R. The impact of energy policies in scenarios on GHG emission reduction in passenger car mobility in the EU-15. Renew Sustain Energy Rev. 2017;68:1088–96. https://doi.org/10.1016/j.rser.2016.02.013.

12. Lodi C, Seitsonen A, Paffumi E, Degennaro M, Huld T, Malfettani S. Reducing CO_2 emissions of conventional fuel cars by vehicle photovoltaic roofs. Transp Res Part D: Transp Environ. 2018;59:313–24. https://doi.org/10.1016/j.trd.2018.01.020.

13. Horowitz CA. Introduction note to Paris agreement. Int Leg Mater. 2016;55:740–55. https://doi.org/10.1017/S0020782900004253.

14. Wei T, Wu J, Chen S. Keeping track of greenhouse gas emission reduction progress and targets in 167 cities worldwide. Front Sustain Cities. 2021;3:1–13. https://doi.org/10.3389/frsc.2021.696381.

15. Fontaras G, Dilara P. The evolution of European passenger car characteristics 2000–2010 and its effects on real-world CO_2 emissions and CO_2 reduction policy. Energy Policy. 2012;49:719–30. https://doi.org/10.1016/j.enpol.2012.07.021.

16. Tsiakmakis S, Fontaras G, Ciuffo B, Samaras Z. A simulation-based methodology for quantifying European passenger car fleet CO_2 emissions. Appl Energy. 2017;199:447–65. https://doi.org/10.1016/j.apenergy.2017.04.045.

17. Hottle T, Caffrey C, McDonald J, Dodder R. Critical factors affecting life cycle assessments of material choice for vehicle mass reduction. Transp Res Part D Transp Environ. 2017;56:241–57. https://doi.org/10.1016/j.trd.2017.08.010.

18. Chen S, Rana R, Haldar A, Ray RK. Current state of Fe-Mn-Al-C low density steels. Prog Mater Sci. 2017;89:345–91. https://doi.org/10.1016/j.pmatsci.2017.05.002.

19. Kim YG, Kim TW, Han JK, Chang RW. Development of new austenitic Fe-Mn-Al-C steels for automotive applications. Key Eng Mater. 1993;84–85:461–71. https://doi.org/10.4028/www.scientific.net/kem.84-85.461.

20. Gutierrez-Urrutia I. Low density Fe–Mn–Al–C steels: phase structures, mechanisms and properties. ISIJ Int. 2021;61:16–25. https://doi.org/10.2355/isijinternational.ISIJINT-2020-467.

21. Zuazo I, Hallstedt B, Lindahl B, Selleby M, Soler M, Etienne A, et al. Low-density steels : complex metallurgy for automotive applications. JOM. 2014;66:1747–58. https://doi.org/10.1007/s11837-014-1084-y.

22. Rana R. Low-density steels. JOM. 2014;66:1730–3. https://doi.org/10.1007/s11837-014-1137-2.

23. Kim H, Suh D, Kim NJ. Fe–Al–Mn–C lightweight structural alloys : a review on the microstructures and mechanical properties. Sci Technol Adv Mater. 2013. https://doi.org/10.1088/1468-6996/14/1/014205.

24. Slater C, Hollyhoke N, Davis C. The influence of alloy composition on the as-cast grain structure in near net shape low-density steels. Ironmak Steelmak. 2017. https://doi.org/10.1080/03019233.2017.1405180.

25. Raabe D, Tasan ÃCC, Springer H, Bausch M. From high-entropy alloys to high-entropy steels. Steel Res Int. 2015;86:1127–38. https://doi.org/10.1002/srin.201500133.

26. Song H, Sohn SSU, Kwak J, Lee B, Lee S. Effect of austenite stability on microstructural evolution and tensile properties in intercritically annealed medium-Mn lightweight steels. Metall Mater Trans A. 2016;47:2674–85. https://doi.org/10.1007/s11661-016-3433-7.

27. Frommeyer G, Brox U. Microstructures and mechanical properties of high-strength Fe–Mn–AI–C light-weight TRIPLEX steels. Steel Res Int. 2006;77:627–33. https://doi.org/10.1002/srin.200606440.

28. Bartlett L, Van Aken D. High manganese and aluminum steels for the military and transportation industry. Jom. 2014;66:1770–84. https://doi.org/10.1007/s11837-014-1068-y.

29. Heo YU, Song YY, Park SJ, Bhadeshia HKDH, Suh DW. Influence of silicon in low density Fe–C–Mn–Al steel. Metall Mater Trans A Phys Metall Mater Sci. 2012;43:1731–5. https://doi.org/10.1007/s11661-012-1149-x.

30. Andersson J-O, Thomas H, Lars H, Pingfang S, Bo S. Thermo-Calc & DICTRA, computational tools for materials science. Calphad. 2002;26:273–312.

31. Thermo-Calc Software AB. TCFE8–TCS steels/Fe-Alloys database, Version 8.0.:1–17.

32. Smetana B, Žaludová M, Zlá S, Dobrovská J, Cagala M, Szurman I, et al. Application of high temperature DTA technique to Fe based systems. Met. 2010-19th Int. Conf. Metall. Mater. Conf. Proc. 2010;357–62.

33. Wielgosz E, Kargul T. Differential scanning calorimetry study of peritectic steel grades. J Therm Anal Calorim. 2015;119:1547–53. https://doi.org/10.1007/s10973-014-4302-5.

34. Perricone MJ, Dupont JN. Effect of composition on the solidification behavior of several Ni–Cr–Mo and Fe–Ni–Cr–Mo alloys. Metall Mater Trans A Phys Metall Mater Sci. 2006;37:1267–80. https://doi.org/10.1007/s11661-006-1078-7.

35. Vandersluis E, Ravindran C. Comparison of measurement methods for secondary dendrite arm spacing. Metallogr Microstruct Anal. 2017;6:89–94. https://doi.org/10.1007/s13632-016-0331-8.